







Nanocrown electrodes for parallel and robust intracellular recording of cardiomyocytes

Zeinab Jahed^{1,2,11}, Yang Yang^{1,11}, Ching-Ting Tsai^{1,11}, Ethan P. Foster ¹, Allister F. McGuire ¹, Huaxiao Yang^{3,4}, Aofei Liu¹, Csaba Forro¹, Zen Yan⁵, Xin Jiang⁵, Ming-Tao Zhao^{3,6,7}, Wei Zhang¹, Xiao Li¹, Thomas Li ¹, Annalisa Pawlosky ⁸, Joseph C. Wu ^{3,9,10} & Bianxiao Cui ¹✉

Drug-induced cardiotoxicity arises primarily when a compound alters the electrophysiological properties of cardiomyocytes. Features of intracellular action potentials (iAPs) are powerful biomarkers that predict proarrhythmic risks. In the last decade, a number of vertical nanoelectrodes have been demonstrated to achieve parallel and minimally-invasive iAP recordings. However, the large variability in success rate and signal strength have hindered nanoelectrodes from being broadly adopted for proarrhythmia drug assessment. In this work, we develop vertically-aligned nanocrown electrodes that are mechanically robust and achieve >99% success rates in obtaining intracellular access through electroporation. We validate the accuracy of nanocrown electrode recordings by simultaneous patch clamp recording from the same cell. Finally, we demonstrate that nanocrown electrodes enable prolonged iAP recording for continual monitoring of the same cells upon the sequential addition of four incremental drug doses. Our technology development provides an advancement towards establishing an iAP screening assay for preclinical evaluation of drug-induced arrhythmogenicity.

¹Department of Chemistry and Stanford Wu-Tsai Neuroscience Institute, Stanford University, Stanford, CA 94305, USA. ²Department of Nanoengineering, Jacobs school of Engineering, University of California, San Diego, CA 92039, USA. ³Stanford Cardiovascular Institute, Stanford University, Stanford, CA, USA. ⁴Department of Biomedical Engineering, University of North Texas, Denton, TX, USA. ⁵Cyion Technologies, LLC, Pleasanton, CA 94566, USA. ⁶Center for Cardiovascular Research, Nationwide Children's Hospital, Columbus, OH, USA. ⁷Department of Pediatrics, The Ohio State University College of Medicine, Columbus, OH, USA. ⁸Google Accelerated Sciences, Google LLC, Mountain View 94043 CA, USA. ⁹Department of Medicine, Stanford University, Stanford, CA, USA. ¹⁰Department of Radiology, Stanford University, Stanford, CA, USA. ¹¹These authors contributed equally: Zeinab Jahed, Yang Yang, Ching-Ting Tsai. ✉email: Bcui@stanford.edu

The waveforms of intracellular action potentials (iAP) reflect the coordination of a multitude of ion channels, some of which are affected by drugs to collectively contribute toward proarrhythmic risks. Parameters including the action potential duration, diastolic interval, rate of depolarization, and the triangulation of repolarization of iAPs, have been shown to serve as predictors of proarrhythmia using human pluripotent stem-cell-derived cardiomyocytes (hPSC-CMs)^{1,2}. The measurement of iAPs is mostly performed by patch clamp, which compares iAP waveforms before and after multi-dose drug treatment from the same cell, i.e. self-referencing. Manual patch clamp is reliable and accurate, but is limited by low throughput and high labor costs. For example, most manual patch clamp studies measure 3–7 hPSC-CMs per drug dose^{3–6}. Several automated patch clamp techniques have been shown to increase the throughput^{7–9}, but these methods require the use of isolated cells in suspension, which disrupts electrically connected cardiomyocytes and may compromise the relevance of the measurement. Even with automated patches, studies usually measure < 10 cells per drug dose^{7,10,11}. Noninvasive and multiplexable microelectrodes can easily achieve parallel recording of extracellular action potentials (eAPs). However, eAPs appear as biphasic spikes and do not provide all critical information for proarrhythmia assessment. Recent microelectrode-based local extracellular action potential method can capture many iAP features, but lacks one-to-one cell to electrode correspondence, is not self-referencing, and the accuracy of measured iAP features is yet to be fully validated by patch clamp^{12–14}.

In the last decade, vertically-aligned and solid-state nanoelectrode arrays (NEAs) have emerged as promising tools with the potential of achieving parallelizable and minimally invasive iAP recording from monolayers of substrate-adhered cardiomyocytes^{15–24}. The recent development of combining vertical nanoelectrodes with CMOS technology has drastically increased the recording throughput of NEAs and has achieved high-throughput recordings in both cardiomyocyte cultures and neuronal networks^{25,26}. Additionally, enabled by integrated current clamp electronics, these methods can now reliably perform intracellular AP recording from neurons which was previously only achievable by patch clamp²⁵. NEA devices differ substantially in their shapes, throughput, and mechanisms of gaining intracellular access. Some devices appear to spontaneously gain intracellular access^{17,20,23,27,28}, while others require transient electroporation^{18,24–26,29,30} or optoporation^{31–33} of the cell membrane. Although spontaneous intracellular access allows iAP recording, it often occurs randomly with a low probability, and cannot be repeated in a controllable manner^{23,24}. On the other hand, transient electroporation of the membrane with a short electric pulse is a controlled method of repeatedly gaining intracellular access and recording iAPs at desired time points. Although all NEAs should be compatible with self-referencing recording, the variable success rate and the short recording duration have largely prevented their usage for multi-dose drug screening. In addition, the fabrication of the majority of nanoelectrodes involve electron beam or ion beam lithography, which are costly and serial processes. These limitations have so far hindered NEAs from being broadly adopted for drug screening purposes.

Other approaches are being developed as surrogate assays for the measurement of iAPs, including voltage and Ca²⁺ optical imaging using fluorescent indicators or genetically encoded molecular probes^{34–36}. These powerful approaches allow simultaneous recording from many cells. That said, some significant drawbacks still exist for optical approaches including the requirement of chemical labeling or genetic modification of cells, photo-toxicity, limited duration of measurement due to photobleaching, and slower on/off kinetics. All these constraints currently prevent them from replacing direct electrophysiological

methods for recording iAPs. Rather, it is often desirable to combine electrophysiological and optical interrogation of the same cell for multimodal analysis, such as correlation between iAPs and calcium transients in cardiomyocytes.

Herein, we developed semi-hollow nanocrown electrodes that are mechanically robust and can perform highly reliable and prolonged iAP recordings. Nanocrown electrodes enable parallel, self-referencing, and multi-dose drug assessment in hPSC-CMs. When combined with a miniaturized recording apparatus housed inside an incubator, these nanoelectrodes will enable iAP-based drug screening.

Results and discussion

Fabrication of robust nanocrown electrode arrays on transparent substrates by photolithography. Our device fabrication process consists of two parts. In the first part of the device fabrication, we developed a protocol to address issues related to the robustness and the fabrication throughput of vertical nanoelectrode arrays (NEAs). In this protocol, photolithography and a top-down dry etching technique were used to fabricate transparent SiO₂ nanopillars (~1 μm in diameter and ~3 μm in height) by directly etching into a SiO₂ substrate (Fig. 1A). These SiO₂ nanopillars are mechanically robust as they are continuous with the substrate at their base. The dry-etching chemistry was optimized to obtain a slightly tapered micropillar profile with a larger diameter and stronger attachment near the base. To reduce the feature size to nanoscale^{37,38}, we employed a wet SiO₂ etching technique that linearly and uniformly shrinks vertical pillars from 1000 nm to 500 or even 200 nm diameter (Fig. 1B). The final diameter is controlled by the duration of the wet etch step. Subsequently, we used photolithography and Pt deposition to pattern conducting electrodes (surrounding the SiO₂ nanopillars) and connecting feed lines. The tapered nanopillar favors the metal coverage and continuity at the nanopillar-substrate edges during metal sputtering. Finally, a thick 600-nm insulating layer of SiO₂/SiN_x was deposited to insulate the entire surface.

In the second part of the device fabrication, the Pt and SiO₂/SiN_x-coated nanopillars were fabricated into either nanopillar electrodes or nanocrown electrodes (Fig. 1A). To fabricate nanopillar electrodes, we used a photoresist-masked dry etching step to selectively remove the insulation layer from the vertical nanoelectrodes. To fabricate nanocrown electrodes, the substrate was first coated with a thick and protective photoresist layer followed by a directional dry etching step to remove both the SiO₂/SiN and the Pt layers from the tip of the nanopillars. Then, the substrate is subjected to a selective and time-controlled wet oxide etching to shorten the SiO₂ core and to remove remaining insulating layers from the pillar. Scanning electron microscopy (SEM) images show the shape of nanopillar (Fig. 1C) and nanocrown (Fig. 1D) electrodes. In these images, the crown top of the nanocrown electrode can be clearly identified, with the conductive platinum layer appearing bright while the insulating SiO₂ core appears dark.

To accurately examine the depth of the crown top, we used focus-ion-beam (FIB) to vertical mill open nanoelectrodes and then used SEM to image their vertical cross sections. From the FIB-SEM cross-section images, the nanopillar electrode shows a uniform platinum coating layer (Fig. 1E), while the nanocrown electrode has a hollow platinum crown 180–200 nm deep for the 3 μm-tall structure (Fig. 1F). We refer to these electrodes as nanocrowns to reflect their shape and the irregular crown rim. Nanocrown electrodes have a lower impedance than nanopillar electrodes (Fig. 1H, Supplementary Fig. 1), likely due to the crown rim that is exposed to the electrolyte on both sides. Compared to the nanopillar nanoelectrodes, the nanocrown

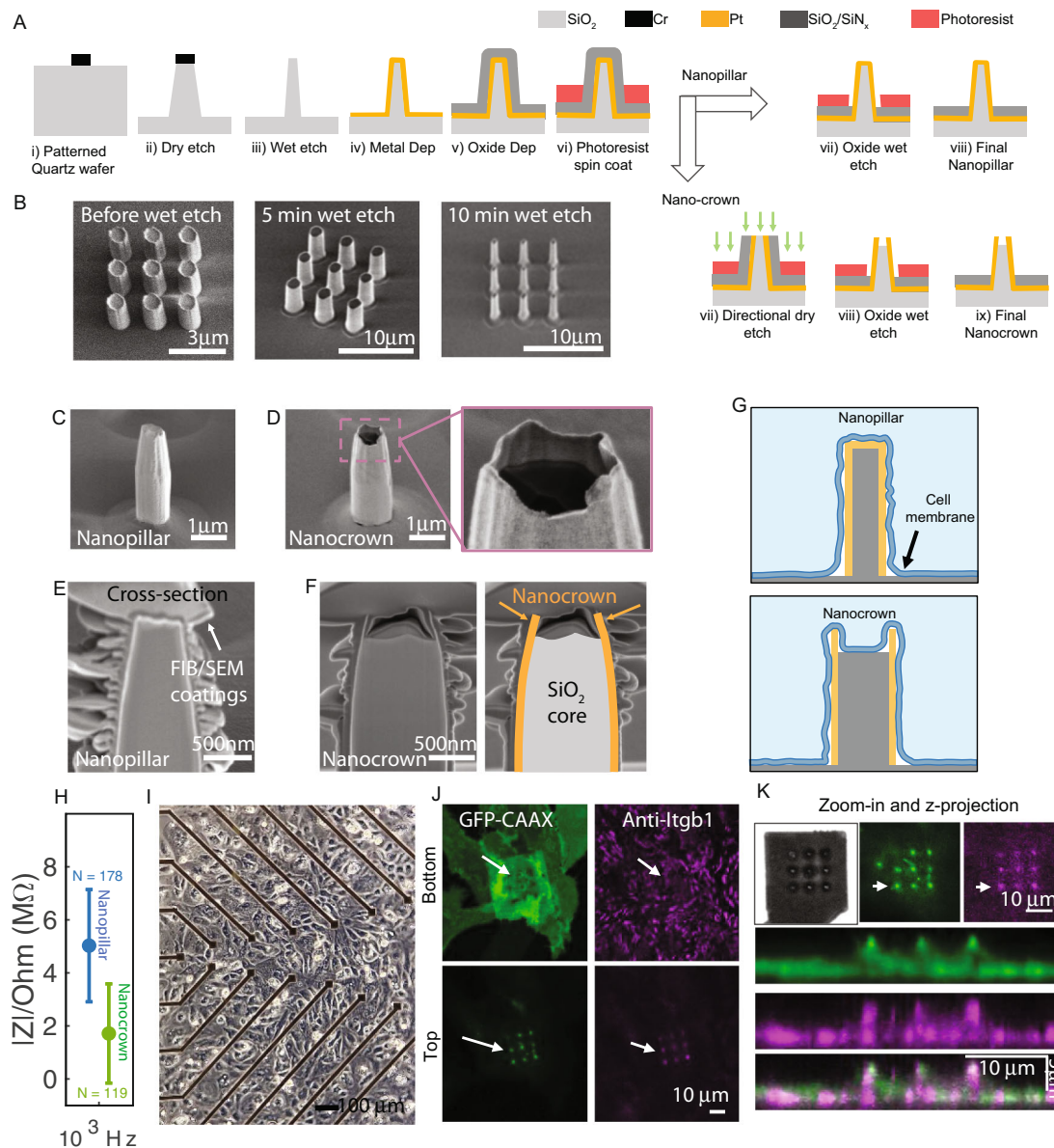


Fig. 1 Fabrication and characterization of robust nanopillar and nanocrown, nanoelectrodes arrays (NEAs). **A** Illustrations of NEA nanofabrication steps. (i) Circular holes were patterned on transparent SiO₂ wafers using maskless photolithography, followed by Cr evaporation. (ii) Reactive ion etching vertically into the SiO₂ substrate to produce slightly-tapered vertical pillars of 700 nm diameters. (iii) pillars were thinned down to 200 nm diameter using a buffered oxide (BOE) wet etch. (iv) Pt metal was sputter coated onto the nanopillars to produce conductive vertical nanopillars. (v) An SiO₂/Si₃N₄ layer was then evaporated onto the surface for insulation. (vi) Photoresist was coated around the nanopillar to protect the insulation layer for subsequent steps. To fabricate nanopillars, an oxide wet etch was used to remove the insulation layer from the pillar tops. To fabricate nanocrown electrodes, first a directional dry etch was used to remove the SiO₂/Si₃N₄ and Pt metal layers from the pillar tips. Next the SiO₂ base of the nanopillar was etched down by a controlled oxide wet etch to fabricate nanocrowns with 50–200 nm depths. **B** SEM images of fabricated pillars before and after thinning with 5-min and 10-min BOE wet etch. **C** SEM image of a nanopillar electrode. **D** SEM image of a nanocrown electrode. **E** SEM image of a focused ion beam (FIB) milled cross section of nanopillar electrodes. **F** FIB/SEM image of nanocrown electrodes (Pt metal crown outlined in orange and SiO₂ in gray). **G** Schematic illustration of the interface of nanopillar and nanocrowns with the cell membrane. **H** Impedance of nanopillar (blue) and nanocrown (green) NEAs at 1 kHz. Data are presented as mean values ± SD. **I** Brightfield microscope image of a monolayer of cardiomyocytes on a NEA device. **J** Confocal images of a cell on a nanocrown electrode, focused on either the top or bottom of the nanocrown. The cell membrane (CAAX:green) and Integrin adhesion proteins (Anti-Itgb1:purple) are seen on top of the nanocrowns (white arrows show location of nanocrowns). **K** Magnified image, and z projection of a cell on top of nanocrown electrodes showing the membrane (green) and integrins (purple) projection along the nanocrown height.

shape will induce the cell membrane to wrap around the outer surface while, at the same time, promotes cell adhesion to the inner core (Fig. 1G). This new shape stabilizes the membrane-electrode interface and is important for repeated and multiple-day recordings. hPSC-CMs were obtained according to our previous protocols^{39,40}. HPSC-CMs cultured on the NEA devices

exhibit spontaneous and rhythmic beating after 2–3 days and can be maintained on the devices for three months or longer (Fig. 1I). We used fluorescence imaging to examine cell adhesions to nanocrown electrodes. For this purpose, we transfected U2OS cells with a membrane marker GFP-CAAX and plated them on an NEA device (Fig. 1J). Unless nanopillar is mentioned

specifically, NEA refers to nanocrown electrode array in the subsequent studies. The cells were fixed and immunostained with anti-activated integrin $\beta 1$ antibody (Sigma-Aldrich) to probe cell adhesions. A bright green dot around the nanocrown electrode indicates that the membrane is wrapping around the vertical nanoelectrodes. The magenta dot around the nanocrown electrode indicates the formation of integrin-containing adhesion complexes. It is worth noting that cell adhesions form on most but not all nanoelectrodes wrapped by the cell membrane. Confocal imaging in the z-direction shows the formation of cell adhesions at the top of the nanoelectrodes (Fig. 1K).

As the new fabrication protocol involves photolithography and is wafer-based, the device throughput and reproducibility are significantly enhanced. Twelve NEA chips fit onto a single 4" wafer and more than a hundred NEA chips can be fabricated in a batch (Supplementary Fig. 2). With each chip consisting of 58 NEA recording pads and two stimulation pads, these NEA devices increase the throughput by enabling parallel recordings and screening across many cell cultures and conditions as we show below. Since we used a SiO₂ substrate, which is effectively a transparent glass surface, these NEAs are compatible with optical imaging and long-term culture of hPSC-CMs.

Nanocrown electrodes enable parallel, reliable, and repeated iAP recordings. Electrophysiology measurements were carried out 5 to 50 days after cardiomyocytes were seeded on NEAs, when cells were in a confluent monolayer and beat synchronously. Before electroporation, NEAs reside outside the cell membrane and record eAPs with a biphasic spike shape and an average amplitude of about ~1 mV, which is similar to that of planar microelectrodes. Upon the application of a single 200- μ s electroporation pulse at ± 3.5 V to a selected nanoelectrode, the recorded action potential transits from an extracellular spike shape to an intracellular waveform (Fig. 2A). When screening the electroporation pulse amplitude ranging from ± 1 to ± 5 V, a ± 3.5 V electroporation pulse resulted in eAP to iAP transition with the highest amplitudes for nanopillar electrodes (Supplementary Fig. 3). In the raw data trace in Fig. 2A, the electroporation event can be easily identified by a sudden rise and temporary saturation of the amplifier. In the same culture, three other nanoelectrodes were simultaneously selected for electroporation. Recordings from these channels showed intracellular recordings while their immediate neighboring channels showed extracellular spikes, indicating that the electroporation and the iAPs were highly localized to the selected nanoelectrodes (Supplementary Fig. 4).

The electroporation-induced extracellular-to-intracellular transition rate is >99%, i.e., almost all eAP signals can be converted to iAPs after a single electroporation pulse delivered through the stimulator/amplifier system (Multichannel Systems, MEA1060-Inv). The amplifier system that we use has limited charge injection capacity and usually limits simultaneous electroporation to 4–6 cells. We will discuss a custom-built amplifier system that allows sequential electroporation from all electrodes in the last section of this article. Multiple rounds of manual electroporation applied to different sets of electrodes allow more iAPs to be recorded at the same time. In a set of experiments shown in Fig. 2B, 15 cells' iAPs were recorded simultaneously. While their beating intervals were identical, these iAPs show differences in their amplitudes, upstroke times, and iAP durations. Amplitude-normalized traces show ~49 ms phase shift in the iAP upstroke time (Fig. 2C). From traces recorded at spatially distinct electrodes, we calculated that the electric signal propagated in the culture dish with a velocity about 0.21 m/s (Supplementary Fig. 5). When these iAPs are aligned to their depolarization upstroke with normalized amplitudes, they

show distinct waveforms and durations despite beating synchronously (for clarity, 4 of the 15 traces were displayed in Fig. 2D). The differences in waveforms are much larger when comparing iAPs from different cultures that are beating at different frequencies (11 iAP traces from 10 different cultures were shown in Supplementary Fig. 6). The differences in iAP duration, shape, upstroke slope, and repolarization form are indicative of intrinsic phenotypic variability among hPSC-CMs, which can be greater than drug-induced effects. Therefore, self-referencing of the same cell is important for assessing drug responses using hPSC-CMs.

In another set of experiments, we demonstrate that the NEA device allows simultaneous iAP recording of 57 hPSC-CMs. Before any electroporation ($t = 0$ –10 s, Supplementary Fig. 7), all channels show extracellular signals except channel 6, which has a defective pin and is always grounded, and channels 13 and 48, which are connected to the two large pads designed for pacing as shown in Supplementary Fig. 2A. Then, we sequentially electroporated all 57 NEA channels that show eAP signals through multiple rounds of manual electroporation. At 15 min ($t = 900$ –902 s), all 57 NEA channels (100%) that were electroporated still show intracellular signals as shown in Fig. 2E.

In addition to simultaneous iAP recordings, nanocrown electrodes allow daily and repeated recording of the same cell over weeks or longer. Figure 2F shows high quality eAP and iAP signals over the time course of 12 days from the same cell. At each date, the culture was first measured for eAP recording, and then electroporated for iAP recording before being placed back in the incubator. In Supplementary Fig. 8, we show recordings from a cell that was repeatedly electroporated and measured for 15 times from day 3 to day 43 after being seeded on the device. These results indicate that long-term iAP monitoring is possible by repeated electroporation and recording sessions.

The extracellular-to-intracellular transition induced by electroporation is due to subnanometer-sized membrane pores that electrically connect NEAs to the intracellular domain. NEA-induced membrane pores are highly localized and reseal over time, during which the recorded signal can appear as a combination of intracellular and extracellular features (Supplementary Fig. 9). We do not consider these juxtacellular signals as intracellular APs. Modeling of the electric fields shows that, during the electroporation step, the electric field is significantly enhanced at the rim of nanocrowns (Supplementary Fig. 10). To probe the size of the membrane pore, we monitored the cellular entrance of calcein, a method often used to probe membrane integrity. Calcein is a membrane impermeable fluorophore about 1 nm in size. We found that calcein was able to get into cells when added 1 min before electroporation, but not when added 1 min or longer after electroporation (Supplementary Fig. 11). This result suggests that the membrane pore has resealed to be less than 1 nm at 1 min after electroporation, when our NEA recording of iAPs usually starts. These membrane pores do not perturb the cell's electrophysiology properties as we show later.

The crown depth critically affects NEA performance. Our results indicate that the depth of the crown significantly affected the electrode performance. In our fabrication process, the depth was controlled by the SiO₂ core etching time. We fabricated nanocrowns of two depths and systematically compared the performance of nanopillar electrodes, 450-nm-deep (~10 min etching time) nanocrown electrodes, or 180-nm-deep (~3 min etching time) crowns. For this study, we recorded 76 cells using nanopillar electrodes, 111 cells using 450-nm deep nanocrown electrodes, and 308 cells using 180-nm-deep nanocrown electrodes, each for a 240 s recording. These measurements were from many independent cultures and pooled together for statistical analysis.

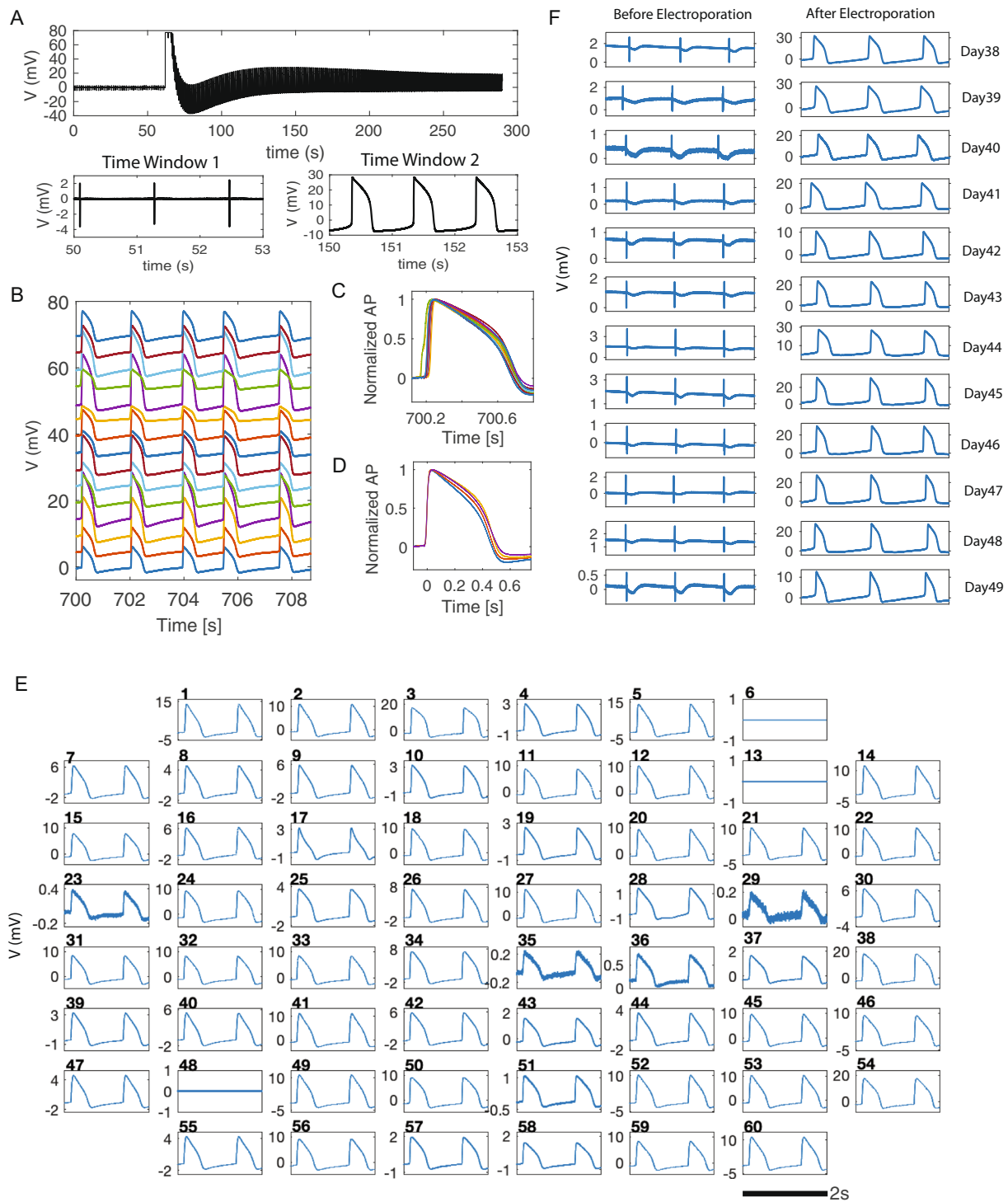


Fig. 2 NEAs enable reliable and noninvasive recording of intracellular action potentials (iAPs). **A** A representative raw trace of NEA recording from a human pluripotent stem-cell-derived cardiomyocyte (hPSC-CM). NEAs measure extracellular action potential (eAP) spikes before electroporation (time window 1), and high amplitude iAPs waveforms after electroporation (time window 2). **B** Simultaneous iAP recordings from 15 NEA channels show synchronous beating of hiPSC-CMs in the same culture. The 3-second traces are vertically shifted for clarity. **C** Overlay of 15 amplitude-normalized iAPs illustrates 40-ms phase shift in depolarization time. **D** Four of the 15 iAPs are aligned to their rising times. They show distinct iAP durations and waveforms for hPSC-CM in the same culture. **E** Simultaneous iAP recording from all NEA channels at $t = 15$ min after many rounds of manual electroporation (excluding channels 6 which is defective, and 13 & 48 which are not NEAs). **F** Twelve daily recording sessions of eAPs and iAPs from the same cell. The recording session started at day 38 on device. For each recording session, eAPs were first measured for 1 min before an electroporation pulse was applied, which converted the signal to iAPs. Each recording session lasted < 30 min and the culture was returned to the incubator afterward. Electroporation-induced membrane pores resealed after every recording session and high quality eAP signals were detected for next recording session.

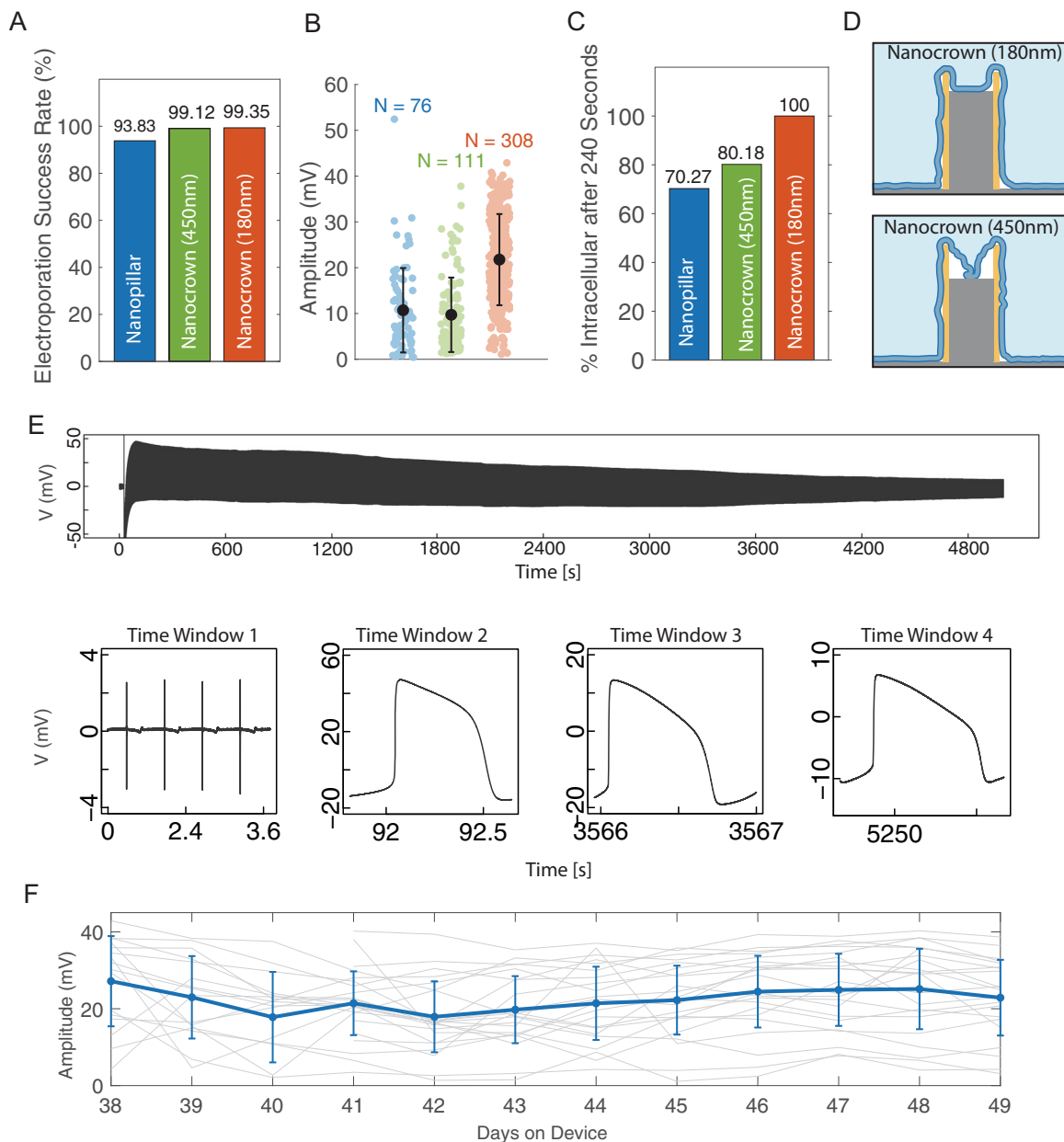


Fig. 3 The crown depth critically affects the Nanocrown electrode performance. **A** Electroporation success rates for Nanopillar electrodes (blue) and Nanocrown electrodes with 450 nm depth (green) and Nanocrown electrodes with 180 nm depth (Orange). Data are presented as mean values \pm SD. **B** The initial amplitudes of intracellular action potentials (iAPs) measured by Nanopillar electrodes (blue), Nanocrown electrodes with 450 nm depth (green) and Nanocrown electrodes with 180 nm depth (Orange). **C** Percent of cells that maintained intracellular access at the end of the recording (\sim 240 s after electroporation). **D** schematic representation of the interface of the cell membrane and the nanocrown electrodes of various depths (450 nm and 180 nm). **E** An iAP recording trace with 180-nm-deep nanocrown shows an iAP amplitude of -63 mV at $t = 1$ min, -30 mV at $t = 1$ h and -16 mV at $t = 1.5$ h. **F** The average iAP amplitude of many cells that are recorded daily remains stable over the 12-day period, indicating that daily-repeated electroporation and resealing cycles do not degrade the recording quality. $n = 16$ cells from three independent cell cultures from day-on-device 38 (DOD38) to DOD49. Six more cells were added on DOD41 for a total of $n = 22$ cells recorded from DOD41 to DOD49. Data are presented as mean values \pm SD.

We define the success rate as the probability of recording intracellular signals shortly after a single ± 3.5 V electroporation pulse, on any cell that exhibits extracellular signals before electroporation (the recording and electroporation protocols and the device model are described in the method section). Both 450-nm-deep and 180-nm-deep nanocrown achieved $> 99\%$ success rate, which was better than the 94% for solid nanopillar electrodes (Fig. 3A). The iAP amplitude measured by 180-nm-deep nanocrown electrodes (21.76 ± 9.95 mV, $N = 308$) is twice as large as that measured by 450-nm-deep nanocrown electrodes (9.7 ± 8.13 mV,

$N = 111$) or by nanopillar electrodes (10.7 ± 9.22 mV, $N = 76$) (Fig. 3B).

When we compare the time-dependent decay of iAPs, 100% of the 180-nm-deep nanocrown electrodes maintained intracellular access at the end of 240 s recording, as compared to 80% for 450-nm-deep nanocrown electrodes and 70% for nanopillar electrodes (Fig. 3C). In another set of experiments, longer 15-min recordings were performed using the 180-nm-deep nanocrown electrodes ($N = 41$). An impressive 100% of these recordings maintained intracellular at the end of 15-min recordings, which was rare for

nanopillar electrodes. This prolonged intracellular access is crucial for pharmacological experiments as we show in the next section. The superior performance of the 180-nm-deep nanocrowns is likely due to the cell membrane forming more stable adhesions to the inner SiO₂ core than that for 450-nm-deep nanocrowns (Fig. 3D). Although we mostly limit our recordings to 15 min to avoid adverse effects to the cells as the culture is recorded outside the incubator, we observe from a few long-recording experiments that the intracellular access duration can be well over an hour for some recordings. For example, the trace in Fig. 3E shows an initial iAP amplitude ~63 mV, which decreases to ~30 mV at 1 hr and is still >16 mV when the recording experiment was stopped at 1.5 hrs.

To systematically investigate how iAP signal changes when a cell is repeatedly electroporated and recorded over many days, we selected 16 cells from three cultures and measured the same cells every day for a total of 12 days from day-on-device 38 (DOD38) to DOD49. Six more cells were added on DOD41 and recorded daily from DOD41 to DOD49. The maximum iAP amplitude is quantified for each recording trace and the amplitudes measured from the same cell are plotted as a gray line in Fig. 3F. Our measurements show that the consecutive daily measurements do not decrease the average amplitude, which remains stable around 20 mV over 12 days (Fig. 3F, Supplementary Fig. 12). These measurements confirm that daily-repeated electroporation and resealing cycles do not degrade the recording quality or perturb cells in the long term. Nanocrown electrodes are mechanically robust because their SiO₂ cores are continuous with the bulk substrate. The nanocrown NEA devices can be repeatedly cleaned and re-used for many cycles of cardiomyocyte cultures. Supplementary Fig. 13 shows the recordings from the same device in six independent cultures over a year. The device performance (signal amplitude and noise) is stable over repeated usage. This remarkable signal stability and device robustness afforded by nanocrown electrodes are not observed using other types of NEA devices.

Simultaneous NEA and Patch recordings from the same cell confirm that NEAs record accurate iAP waveforms. To determine the accuracy of iAP waveforms recorded by NEAs, we compared these measurements with those recorded by manual patch clamp, which is the gold standard of intracellular recording. In these experiments, we performed simultaneous patch clamp and NEA recordings on the same cell (Fig. 4A). The transparent substrate allowed us to identify hPSC-CMs in contact with NEAs under a microscope for manual patch clamping (Fig. 4B). Upon obtaining a high seal resistance with the patch pipette, suction was applied through the pipette to breach the membrane and thus allowing iAPs to be recorded by the patch electrode. Before applying the electroporation pulse at $t = 0$, the patch electrode recorded typical iAP waveforms, while the simultaneous NEA electrode recorded characteristic eAP spikes (Fig. 4C, D). After NEA electroporation, both the patch and the NEA electrodes showed intracellular AP waveforms, albeit with different amplitudes (Fig. 4D). The electroporation event showed up as a sudden rise and saturation of amplifiers in both NEA and patch traces, which was used to align the two time traces. We note that sudden decrease of patch iAP amplitude due to loss of sealing resistance is common in patch recordings from cardiomyocytes that were not cultured on nanoelectrodes (Supplementary Fig. 14). Electroporation-induced decrease of patch iAPs is due to a reduction in the patch sealing resistance, not a change of the resting membrane potential, which would have dramatically affected the cell's propensity to fire action potential and the refractory interval duration. As we show in the next section, the

cycle time and the diastolic interval are not affected by the electroporation.

We wrote software to automatically calculate a single scaling factor for each pair of patch- and NEA-recorded iAPs to account for the difference in their amplitudes. The scaled and overlaid iAP traces show that the two waveforms almost entirely overlap (Fig. 4E). We carried out the simultaneous patch and NEA dual recordings for a total of 10 cells, all showing near-perfect overlap after scaling (see Supplementary Fig. 15 for 8 more examples of dual-recording traces). From iAPs recorded by NEA and patch, we calculated a set of parameters known to be related to drug-induced proarrhythmia (Fig. 4F). These parameters included cycle time, diastolic interval (time interval where the membrane potential is more negative than 90% repolarization), action potential durations APD90 and APD50 (time taken to reach 90% and 50% of repolarization, respectively), and t_{rise} (the depolarization time from APD80 to APD20). Despite large variations among individual cells for each parameter, recordings of Patch and NEA from the same cell agree nearly perfectly with each other (Fig. 4G). Averaging over the 10 experiments, the differences between NEA and patch measurements were minimal: $0.05 \pm 0.08\%$ for cycle time, $0.8 \pm 0.6\%$ for APD90, and $3.21 \pm 2.10\%$ for APD50, $0.85 \pm 0.65\%$ for diastolic intervals, and $6.67 \pm 9.75\%$ for t_{rise} (Fig. 4H). The comparison of simultaneous Patch and NEA recordings confirm that NEAs provide accurate measurement of iAP waveforms and parameters.

NEA records accurate iAP waveforms despite time-dependent decrease of the iAP amplitude. Resealing of the electroporation-induced membrane pores over time causes the amplitude of NEA-measured iAPs to decrease over time. In the trace shown in Fig. 5A, the NEA iAPs decrease by an order of magnitude from 14 mV at 60 s to 1.3 mV at 530 s after electroporation. In the same time period, the patch iAPs from the same cell first increased and then exhibited large fluctuations after 430 s. The zoom-in plots show 15-s windows at three time points, $t = 0, 80,$ and 430 s, for both patch and NEA traces (Fig. 5B). From the patch trace around $t = 0$ s, we can clearly see that the amplitude of the patch iAP is reduced from 95 mV to 35 mV upon electroporation at $t = 0$ s. Despite the drastic change in the patch iAP amplitude, the cycle time is unperturbed and the overall iAP waveform remains the same. The NEA trace shows extracellular spikes before electroporation and then is out of range immediately after electroporation because of the amplifier saturation. In the $t = 80$ s zoom-in window, the NEA electrode has recovered and both patch and NEA electrodes record iAPs that are synchronized in time and show similar waveforms but with different amplitudes. In the $t = 430$ s zoom-in window, the patch iAP shows a sudden decrease in amplitude at $t = 432$ s, likely due to a decrease of the patch sealing resistance. The event shows as a slight change of the baseline in the NEA channel without changing the iAP amplitude or the waveform.

We developed a software package that automatically detects the spiking point (red stars), the starting point (green stars), the maximum point (blue stars), and the minimum point (cyan stars) of each iAP in the entire trace. A few iAPs immediately after the electroporation are omitted from analysis as there are often spurious artifacts. From these identified points, the software calculates the time-dependent evolution of cycle time, diastolic interval, APD90, APD50, amplitude, and spike velocity (dV/dt). Detailed analysis of traces shown in Fig. 5A is presented in Fig. 5C. Detailed analysis of traces shown in Fig. 4C is included in Supplementary Fig. 16. The analysis results show that the cycle time and the diastolic interval remain the same before and after electroporation despite the dramatic change of the amplitude.

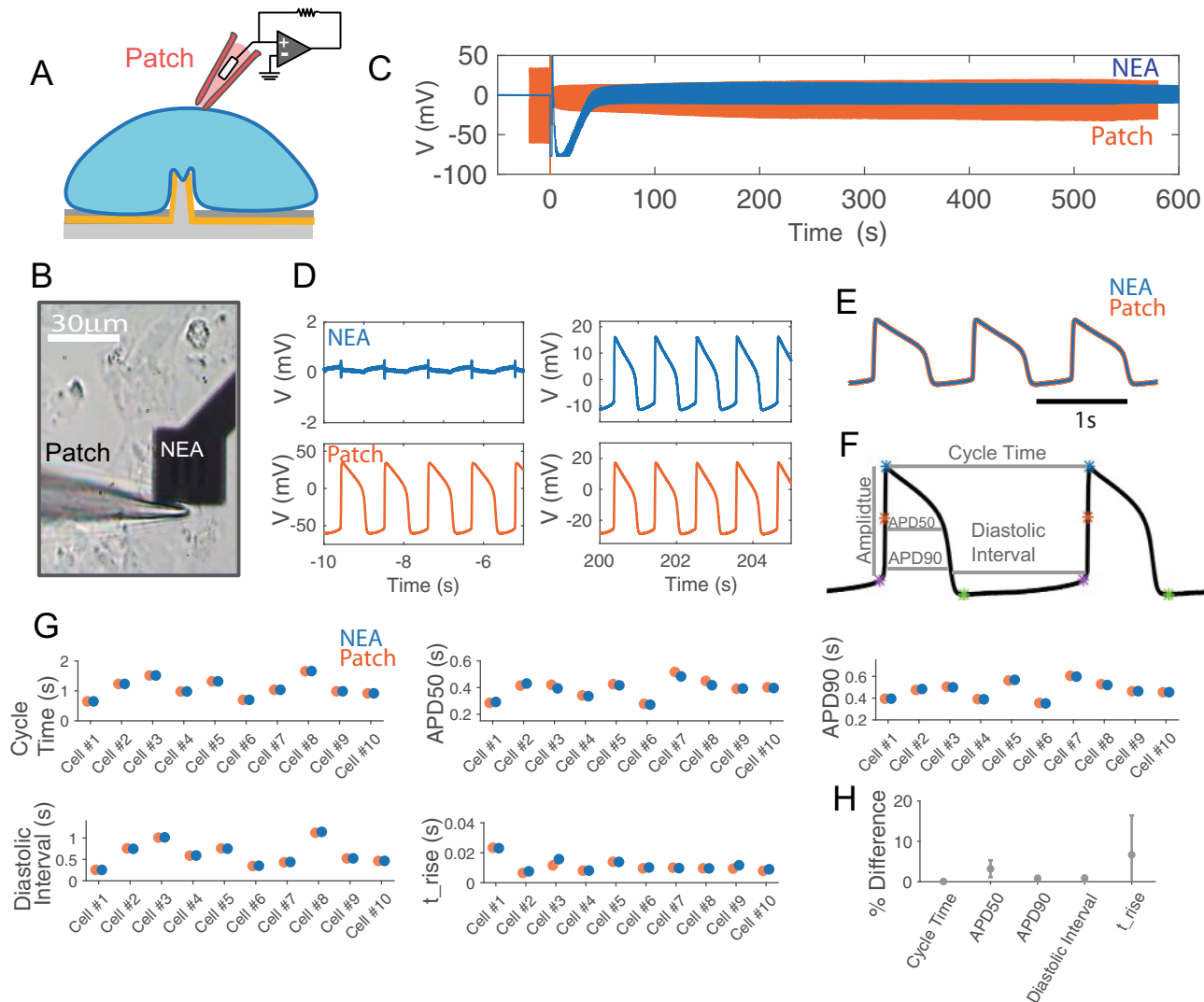


Fig. 4 Simultaneous Patch clamp and nanoelectrode array (NEA) recordings verify the accuracy of NEA-recorded intracellular action potentials (iAPs).

A A schematic representation of simultaneous patch and NEA recording from the same cell. **B** A brightfield image showing a patch pipette approaching a cell on the nanopillar electrode from the left. **C** Simultaneous recording traces by patch clamp (orange) and NEA (blue) from the same cell. The two traces are aligned in time with $t = 0$ for electroporation. **D** Zoomed-in time windows of NEA- and Patch- recordings before electroporation (left) and after electroporation (right). Before electroporation, NEA measured eAP spikes while patch clamp measured iAPs with high amplitudes. After electroporation, both NEA and patch measured iAPs. **E** Three pairs of NEA- and Patch-recorded iAPs are amplitude normalized and overlaid together. The overlays show identical waveforms. **F** Analyzed features of iAP waveforms: APD50, APD90, cycle time and diastolic interval and amplitudes. **G** Deviations of iAP features between NEA- and patch-recorded iAPs for ten independent cells. **H** Averaged values of deviations of iAP features between NEAs and Patch for $N = 10$ cells. Data are presented as mean values \pm SD.

Therefore, the physiological functions of cardiomyocytes are not perturbed by NEA-delivered electroporation. APD90 and APD50 are slightly decreased immediately after electroporation but remain stable afterward. For the NEA trace, APD90 and APD50 remain constant for the entire time despite an order of magnitude decrease in amplitude. On the other hand, the amplitude and the spike velocity, which is dependent on the amplitude, show large changes. We note that, when the electroporation pulse is delivered simultaneously to many NEA pads, e.g., > 30 , it sometimes stimulates the whole culture and reduces the cycle time regardless of whether a cell is electroporated or not.

To further confirm that the patch and NEA iAP waveforms are not dependent on their amplitudes, we presented the scaled and overlaid iAPs at four different time points (Fig. 5D). During the time period, the patch iAP amplitude increased from 71.81 mV to

92.68 mV and then decreased to 81.39 mV. The NEA iAP amplitude decreased by about an order of magnitude from 12.76 mV ($t = 80$ s), 5.17 mV ($t = 300$ s), 2.28 mV ($t = 430$ s), and 1.36 mV ($t = 530$ s). Despite their dramatic differences in amplitudes, the pairs of iAPs at the same time overlay nearly perfectly. The overall waveform deviation between paired Patch/NEA iAPs (Fig. 5E) and the APD90 deviation (Fig. 5F) are $\sim 1\%$ for the entire period, which is negligible as compared to the drug effects we show later. From a simplified circuit model (Supplementary Fig. 17), both patch and NEA signals are linearly dependent on the biological signal, which explains why they report the same iAP waveform despite differences in amplitudes.

NEA enables self-referencing assessment of drug-induced changes of iAPs. As shown in Supplementary Fig. 5 and in the previous studies⁴¹, hPSC-CMs are mixed populations with cells

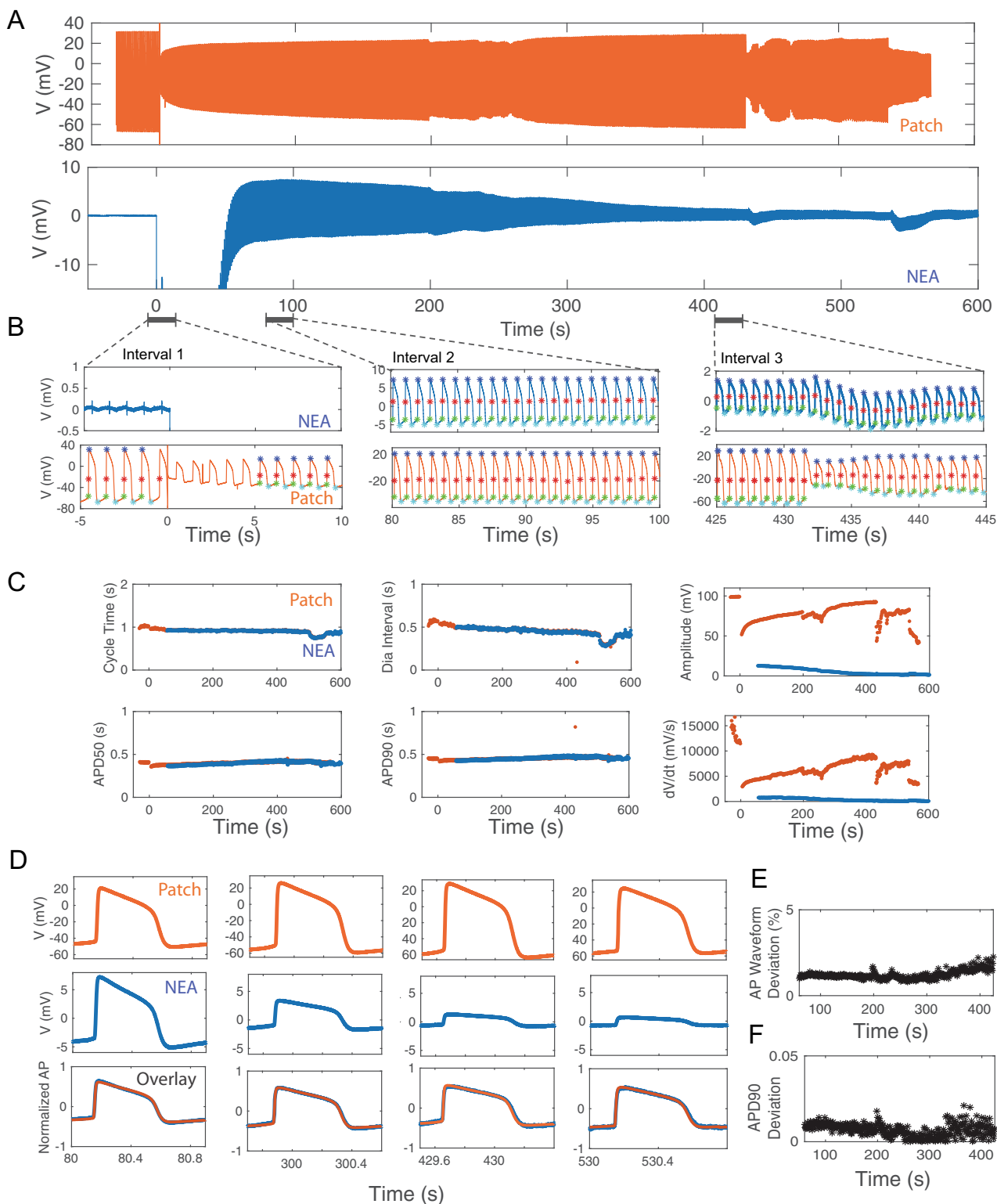


Fig. 5 Comparison of APD features in simultaneous Patch clamp and nanoelectrode arrays (NEA) recordings. **A** Simultaneous recording traces by patch clamp (orange) and NEA (blue) from the same cell. The two traces are aligned in time with $t = 0$ for electroporation. **B** Zoomed-in time windows of NEA- and Patch- recordings directly before and after electroporation (Interval 1), 80 s after electroporation (Interval 2), and 425 s after electroporation (Interval 3). The significant points on each iAP include spiking (red stars), starting (green stars), maximum (blue stars), and the minimum (cyan stars) points which are determined automatically by our in-house software. **C** Overlay of time-dependant changes in action potential duration (APD) features calculated using the Patch (Orange) or NEA (blue) recordings including cycle time (s), APD50 (s), APD90 (s), diastolic interval (s), amplitude (mV) and spiking velocity- dV/dt (mV/s). **D** Comparison of iAP amplitudes between patch (top-orange) and NEA (middle-blue) recordings at four time intervals after electroporation (80 s, 300 s, 430 s, and 530 s). As the membrane pores sealed over time, the amplitude of NEA-recorded iAPs decreased. Nevertheless, the scaled NEA and Patch recordings (Bottom row) largely overlap at various time intervals. **E** Time dependent deviations of AP waveforms of patch and NEA recordings. **F** Time dependent deviations of APD90 calculated from patch or NEA recordings.

showing heterogeneous iAP waveforms. Furthermore, the iAP waveform is affected by the cell density, beating frequency, and culture conditions⁴². The variability among iAPs underlined by phenotypical and physiological differences between cells and cultures can be much larger than drug-induced effects on a given cell's iAP. This necessitates self-referencing - comparing the before-drug and after-drug iAPs in the same cell. Indeed, the standard patch clamp-based drug assay is self-referencing. However, the patch clamp method is labor intensive, low throughput, and not suitable for drug screening in hPSC-CMs.

NEAs enable self-referencing measurements of drug effects in parallel. For this study, we used NEAs to test a number of compounds with known arrhythmogenic risk selected from the CiPA library^{2,43} using common protocols in conventional pharmacology methods with patch clamp³. After electroporating and obtaining stable iAP signals, we first added DMSO as a vehicle compound (Fig. 6A). Subsequently, with continuous iAP recording, four increasing doses of a selected drug (dissolved in DMSO) were sequentially added to the cell culture every 3–4 min (0.3 nM, 1 nM, 3 nM, 10 nM of dofetilide for the trace shown in Fig. 6A). The mechanical agitation caused by liquid exchange induced signature fluctuations both in the measured channel and in the non-electroporated control channels, which we used to indicate the drug addition time. In each trace, 1000–2000 intracellular APs were recorded during the 15–20 min recording period (Fig. 6A).

Using self-referencing NEA recordings, we compared a group of common high, low and medium risk compounds that are known to distinctly alter the shape of iAPs (Fig. 6B). High-risk compounds such as dofetilide and D,L-sotalol are known to prolong iAP durations, while low-risk compounds such as verapamil and nifedipine reduce iAP durations^{44–46}. To examine drug effects, action potentials were selected for analysis 3-min after each dose addition. Action potentials from the same cell were normalized and aligned to their depolarization phase. By self-referencing, drug-induced prolongation of the action potential duration is clearly visible for dofetilide and D,L-sotalol (Fig. 6B). On the other hand, drug-induced shortening of the action potential duration is evident for verapamil and nifedipine (Fig. 6B). Another compound, cisapride induced early-afterdepolarization events. These data shows that NEAs are able to reliably capture drug-induced effects by self-referenced recordings.

Interestingly, after analyzing many cells, we found three types of dose responses to Dofetilide. This is represented in Fig. 6C which shows 3s zoom-in windows of the raw iAP traces at 60 s, 600 s, and 900 s. For the first response type, increasing doses of dofetilide at 0.3, 1, 3, 10 nM cause a monotonic dose-dependent increase of APD90 with the iAPs getting wider with increasing drug doses, but the fast uprisings of the depolarization phase remains similar (represented ~50% of cells). For the second type that represented 30% of cells, the highest dose caused shortening of APD90, i.e. refractory dosage at 10 nM. For the third type, the medium dose of 3 nM already caused shortening of APD90, i.e., refractory dosage at 3 nM. For the second and the third types after the refractory dosage (10 nM for the second type and 3 nM for the third type), the iAP duration gets narrower but the shape is drastically different from the narrower iAPs at lower doses. In particular, the uprisings duration is longer and the overall waveform is more triangularized. For cell 2, some action potentials are missing after 900 s.

Quantification of APD90, APD50, t_{rise} , and triangulation (APD90-APD30) highlights the variabilities of drug-induced responses in different cells and the importance of self-referencing in identifying these variations (Fig. 6E). The unique advantage of NEAs for drug assessment is that one can measure iAPs at

multiple drug doses from the same cell and measure the responses of multiple cells in the same experiment. In this way, a set of dose-response data can be obtained with self-referencing to avoid the large cell-to-cell and culture-to-culture variations inherent to hPSC-CMs. APD90 and APD50 are often used for assessing drug effect. In a couple of days, we were able to measure 84 self-referencing dose-response curves using independent cultures (Fig. 6E). Membrane pores on some of these cells were sealed before higher doses were added, so there are fewer data points for higher doses, for example, $N = 84$ for the control and $N = 40$ for the highest dofetilide concentration at 10 nM (Fig. 6E). Nevertheless, the $N = 40$ per dose sample size is already significantly larger than previous studies reporting iAP dose-response measurements with $N < 10$. From the APD90 plot, it is obvious that some cells show monotonic dose-dependent increase, while others show refractory dosage at 3 nM or 10 nM. It is interesting that, for cells that show decreased APD90 after the refractory dosage, their t_{rise} parameter shows significant increase (Fig. 6E).

Unlike patch clamp or other invasive iAP recording methods in which the cells are no longer viable after recording, the NEA measurements are minimally invasive. Therefore, after washing out drugs and allowing 1–2 days of recovery in the incubator, the same hPSC-CM culture can be used again for assessment of the same or different drugs. In one experiment, we showed the dofetilide dose-responses from the same culture at day 1, day 3, and day 4, with the three independent sets of experiments showing slightly different drug effects induced by dofetilide (Supplementary Fig. 18). The fact that the same hPSC-CM culture can be used repeatedly for multiple drug assessment experiments reduces the number of precious hPSC-CM cell cultures required for obtaining dose-response curves, thereby facilitating the drug screening process.

In-situ recording using miniaturized Petri-dish-like recording stage.

All the data shown earlier were collected using a commercially available amplifier (MEA 1060, MCS), which requires that the culture be taken out of the incubator and placed on the recording stage for electrophysiology measurements. The health and the electrophysiological properties of cardiomyocytes are sensitive to experimental conditions such as temperature, humidity, and CO₂ level^{47,48}. To reduce environmental variabilities, we recently collaborated with Cyion Technologies to design a miniaturized recording stage for in situ long term recording inside a CO₂ incubator, which is controlled through a cable connected to a computer outside the incubator. The printed circuit board hosting our NEA devices was fitted with a bottomless 35 mm Petri-dish (Fig. 7A, B). In this design, the Petri-dish is placed on the recording stage with a short distance between the cell and the amplifier to minimize signal loss or distortion (Fig. 7C). In situ recording significantly reduced temperature-dependent variations in the cells' electrophysiological behavior. Immediately after a culture was taken out of the incubator and mounted on a recording stage, we often observed a significant change in the cycle time, which is known to be affected by temperature⁴⁸ (Fig. 7D). By comparison, the cycle time was much more stable when using our custom recording stage housed inside the incubator. The Cyion amplifier stage and custom-made software also supports automated sequential electroporation of all NEA channels in < 1 s with the potential for simultaneous iAP recording of up to 58 channels. Therefore, the miniaturized Petri-dish-like recording stage is ideally suited for iAP recordings. These new capabilities further enhance the advantage of using NEAs for preclinical evaluation and screening of new drug candidates in hPSC-CMs.

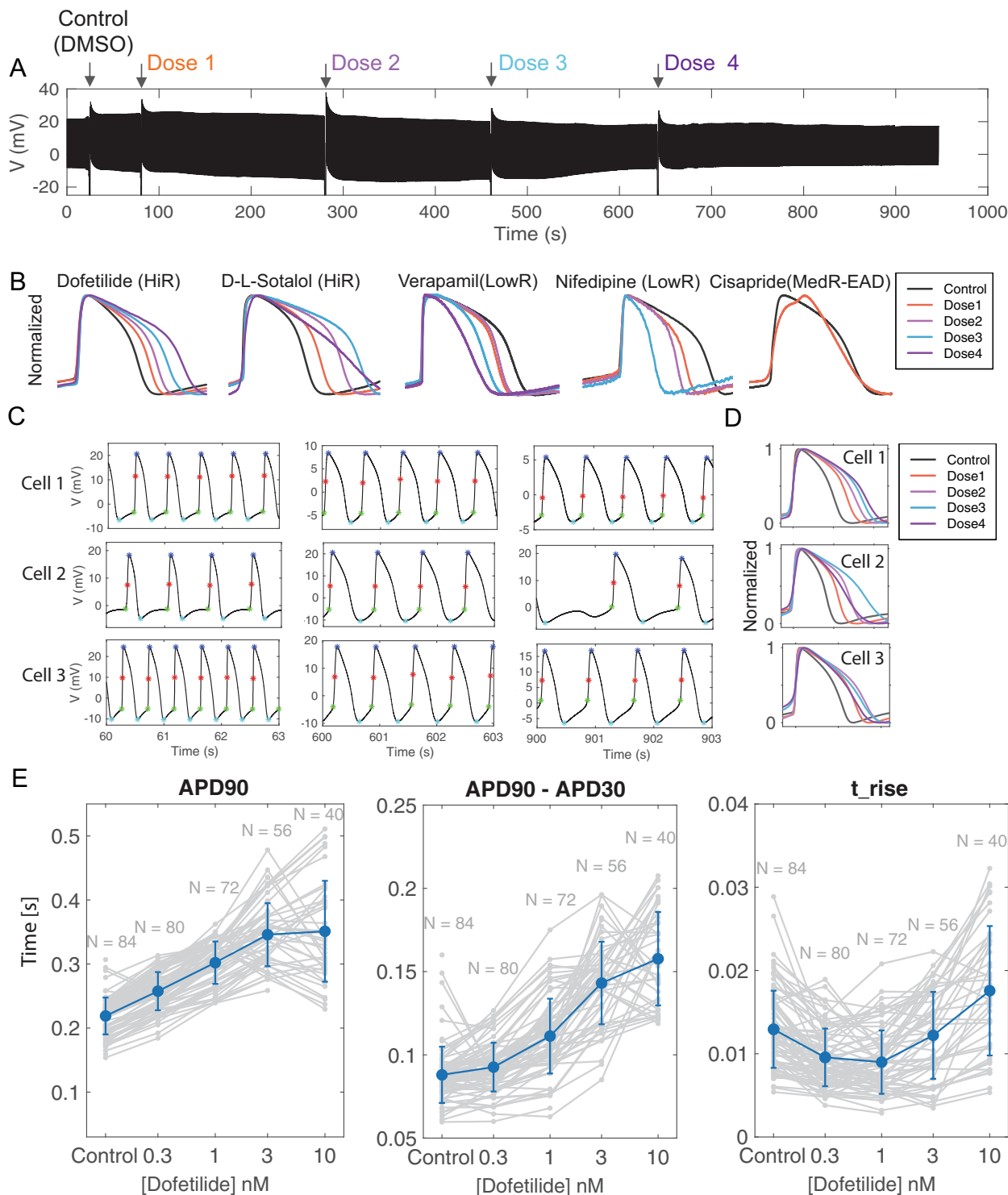


Fig. 6 Self-referencing assessment of pharmacological compounds using nanocrown electrodes. **A** A raw data trace of intracellular action potentials (iAPs) with sequential addition of pharmacological compounds (Dofetilide for the displayed trace). DMSO is added first as a control, after which an increasing dose of the selected drug is added every 3–4 min while iAPs are continuously being recorded. The large variations in the signal trace are due to vibrations associated with exchanging lipids when new doses of the drug are added (indicated by arrows). **B** Overlay of amplitude-normalized and self-referencing iAPs, i.e., the same cell before and after adding increasing doses of each drug. The high risk drugs Dofetilide and D,L-Sotalolol caused dose-dependent prolongation of iAPs, while the low-risk drugs Verapamil and Nifedipine caused dose-dependent shortening of iAPs. The medium-risk drug Cisapride caused early after-depolarization (EAD). The increasing doses for each drug (Dose1, Dose2, Dose3, and Dose4) were as follows: Dofetilide (0.3 nM, 1 nM, 3 nM and 10 nM), D-L-Sotalolol (0.1 μM, 1 μM, 10 μM, 100 μM), Verapamil and Nifedipine (1 nM, 10 nM, 100 nM, 1000 nM), and Cisapride (1 μM). **C** Dose-dependent changes in APD 90 for three cells showing distinct responses to Dofetilide. iAP waveforms at various time points during the pharmacology experiments at 60 s (DMSO), 600 s (Dose3), and 900 s (Dose4) are shown. **D** Self-referencing iAPs alignments for cells 1, 2 and 3 show different dose-dependent responses to Dofetilide at doses 3 and 4. **E** Self-referencing iAPs from 40–84 cells show dose-dependent changes in APD90, APD90-30 (triangulation), and rising time in response to Dofetilide. Data are presented as mean values ± SD.

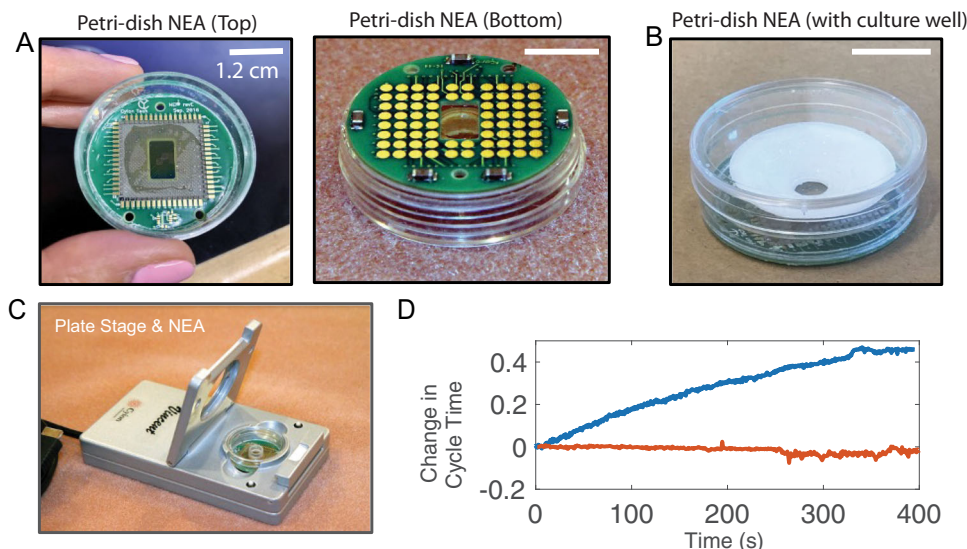


Fig. 7 In-situ iAP recording using miniaturized petri-dish-like recording stage. **A** Photographs of a Nanocrown device bound to a printed circuit board and integrated with a bottomless 35-mm petri dish. When placed on the recording stage, the electrode pads at the bottom are in contact to pogo pins inside the stage. **B** A plastic 3D printed well (white) is assembled on top of the petri-dish NEA for cell culture. **C** The petri dish NEA is situated in a Cyion recording stage. The recording stage is housed inside a CO₂ incubator for in-situ recording. **D** The measured cycle time of beating human pluripotent stem-cell-derived cardiomyocytes (hPSC-CMs) gradually increases over 400 s on the MCS recording stage (blue trace, outside the incubator), while the measured cycle time remains stable when using the miniaturized Cyion stage (orange trace, inside the incubator).

In summary, we presented the development of semi-hollow nanocrown electrodes. The crown shape induces the cell membrane to wrap around the outer surface and adhere to the inner core, which stabilizes the membrane-electrode interface. Nanocrown electrodes achieve 99% electroporation success rates and reliably measure iAPs from cardiomyocytes with high accuracy and signal strength. The prolonged recordings allowed us to perform a series of pharmacology experiments based on the self-referencing iAP waveform. The development of a Petri-dish NEA and an accompanying miniaturized recording apparatus would enable in situ recording of iAPs inside CO₂ incubators. These developments will hopefully enable iAP-based assays for dose-dependent drug screening.

Methods

Nanopillar and Nanocrown electrode array fabrication. Quartz wafers were cleaned and deposited with HMDS to promote photoresist adhesion. A positive photoresist (Shipley 3612) was spin-coated and exposed by a maskless aligner (Heidelberg MLA-150) to pattern circular holes. A Cr mask of 120 nm was later deposited by metal evaporation before being lifted-off in acetone to make circular Cr disks. Using the deposited Cr as a mask, vertical microstructures were subsequently generated by anisotropic reactive ion etching with a mixture of C4F8, CHF3, and Ar (Versaline LL-ICP Oxide Etcher) to precisely control the vertical profiles of the quartz nanostructures. The substrates were then immersed in Chromium Etchant 1020 (Transene) to remove the chrome mask and subsequently wet-etched in Buffered Oxide Etchant (BOE) 20:1 (Transene) to decrease the nanostructures' dimensions. For electrode fabrication, a bilayer resist strategy was used to construct metal connection lines with smooth edges. Microposited LOL and Shipley 3612 were spin-coated, baked, and then exposed to create an undercut in the Microposited LOL layer underneath the resist for the lift-off step. A layer of Ti (10 nm) and Pt (40 nm) was sputtered and then lifted-off in Microposit Remover 1165 for 16 h. Subsequently, the insulation layers composed of 60 nm of Si₃N₄ and 540 nm of SiO₂ were deposited via plasma-enhanced chemical vapor deposition (350 °C; Plasma-Therm Shuttlelock).

For nanopillar electrodes, the insulation layer was removed from the nanopillars through the spin coating of a thin layer of resist, followed by a wet etch in Buffered Oxide Etchant 20:1 (Transene). For nanocrown electrodes, a semi-hollow conversion strategy was applied after the insulation step to create nanocrowns. Briefly, a layer of photoresist was spin-coated to protect the entire substrate. Then, the substrates were anisotropically etched with Ar (MRC model 55 RIE) to remove the insulation layer and the metal layer at the tip of the nanostructures and expose the inner quartz. The inner quartz core was subsequently etched with BOE. The depth of the nanocrown was controlled by varying the etching time between 3 to 10 min. Nanocrowns with 450 nm or 180 nm crown depths were fabricated by 10 min or 3 min BOE etching, respectively. Finally, the quartz wafers were diced

into 12.5 mm × 12.5 mm pieces by the Micro Dicing Services to fit our custom made printed circuit boards. The final devices were characterized by SEM (FEI Nova). For each of the 12 NEA devices fabricated on a wafer, nanoelectrodes on all 58 channels were observed under the SEM before assembling the device on a custom made printed circuit board (Fig. 1b–f shows one representative image of hundreds of imaged nanoelectrodes). We made over 40 NEA devices (each with 58 nanoelectrodes) reproducibly using our nanofabrication technique.

hPSC-CM differentiation. hPSC-CMs were differentiated and purified based on our previously developed protocols^{39,49,50}. Briefly, hPSCs (line SCVI-273) with 90–95% confluency were treated with 6 μM CHIR99021 (Selleck Chemical) in RPMI (Gibco®, Life Technology) supplemented with B27 w/o insulin for 2 days, and allowed to recover for 1 day in RPMI plus B27 without medium. Then cells were treated with 5 μM IWR-1 (Selleck Chemical) for 2 days. After recovering in the fresh RPMI plus B27 without insulin medium for another 2 days, cells were switched to RPMI plus B27 with insulin for 2 days. Beating hPSC-CMs were derived around 9–11 days after differentiation. The hPSC-CM were purified with glucose-free RPMI plus B27 with an insulin medium for 2–4 days. Differentiated hPSC-CMs were maintained in RPMI plus B27 with insulin medium for the following experiments.

Immunostaining of cell adhesions. The samples were incubated with 1:100 diluted anti-activated integrin β1 antibody (Sigma-Aldrich, MAB2079Z) in HEPES-Buffered Hanks Balanced Salt Solution (HHBSS), for 30 min at 4 °C. The samples were then washed with ice-cold HHBSS for 3 times and fixed with 4% Paraformaldehyde in PBS for 15 min at room temperature (RT). The fixed samples were washed with PBS for 15 min and incubated in blocking buffer (5% Bovine serum albumin in PBS) for 1 h at RT. The sample were then incubated with 1:500 Alexa Fluor 488-conjugated goat anti-Mouse IgG (H + L) secondary antibody (Thermo Fisher Scientific, A11001) in blocking buffer at RT for 45 min, washed with PBS for 15 min at RT. The experiments were performed on 2 devices and images were taken of 59 pads in total. Among these, 44 out of the 59 imaged pads exhibit similar effect as shown in the representative images in Fig. 1i–k.

Cell Culture of hPSC-derived-CMs on NEA devices. hPSC-CMs were maintained in Matrigel pre-coated 6-well plates in RPMI 1640 medium (Gibco REF 500 ml) with B-27 supplement (Gibco REF 10ml). The culture medium was refreshed every 2–3 days. Before seeding cells on NEA devices, the devices were coated with 1 mg/ml poly-L-Lysine at room temperature for 15 min, 0.5% Glutaraldehyde in PBS at room temperature for 10 min, and followed by 1:200 Matrigel (Corning REF 356231) in DMEM/F12 (Gibco REF 10565-018) at 37 °C for 3 h or overnight. A three times PBS wash was performed between each coating step. Cells were dissociated with TryPLE select 10X (Gibco REF A12177-01) at 37 °C for 5 min and ~12 × 10⁵ cells were plated in each coated device in culture medium supplemented with 10% KnockOut Serum Replacement (KSR)(Gibco REF A31815-01), and cultured in a 5% CO₂ incubator at 37 °C. The medium was refreshed with normal culture medium every 1–2 days from the second day after replating. Cells are maintained in regular cell culture medium

before and after electroporation and during recording. Measurements were done 5–30 days post-plating unless otherwise stated. The devices are reusable after the following washing steps in the device wells: 5 min of incubation with TrypLE Express (Gibco REF 12605-028) at 37 °C to remove cells, overnight incubation with Enzymatic cleaner (Ultrazyme) in PBS at room temperature, and leave in 70% ethanol for at least 1 h. The wells are always immersed in 70% ethanol until the next usage. The devices were dried of ethanol and further decontaminated with UV illumination for 30 min before coating for the next cell culture.

Electrophysiology recordings. All recordings were performed by a 60-channel voltage amplifier (MEA1060-Inv-BC, Multi-Channel Systems, Reutlingen, Germany), equipped with a plate heating system which was maintained at 37 °C for all recordings. Recordings were performed at a sampling rate of 5 kHz. Simultaneous patch-clamp and NEA recordings were carried out on hPSC-CM at room temperature in the culture medium (RPMI 1640 + B-27). For patch-clamp, the action potential was recorded under whole-cell current-clamp mode using Multiclamp 700B amplifier and Digidata 1440 A digitizer (Axon Instrument) with pClamp10 software (Molecular Device). Borosilicate patch pipettes (Sutter Instruments, O.D.: 1.5 mm, I.D.: 0.86 mm) were pulled with a P1000 pipette puller (Sutter Instrument) with resistances between 2 and 6 MΩ. Pipette internal solution contains in mM: 120 K Aspartate, 20 KCl, 1 MgCl₂, 5 EGTA-KOH, 0.1 CaCl₂, 10 HEPES, 4 Mg₂ATP. The pH was adjusted to 7.20 with KOH. The patch-clamp recording was done at 10 kHz sampling rate and a 10 kHz Bessel filter was applied. During the experiments, cells occupying NEA pads were located through a microscope. The extracellular signal recording was initiated on NEA followed by patching of the cell. After action potential signals were observed through patch-clamp, electroporation was applied to the same cell through nanoelectrodes to get the intracellular signal. Recordings from both NEA and patch electrodes started before the electroporation and continued during and after the electroporation. Data analysis was performed with Matlab and Python as stated below.

Electric field models. To assess the difference in electric field strength between hollow and full nanopillars, we performed a finite-element analysis of the voltage distribution in 3D in vacuum. We did not simulate the electrolyte and double-layer effects for simplicity. Therefore, the obtained results can qualitatively translate only to the electric field strength during fast transients when operating the nanopillars in electrolytes. We used FEniCS, a Python implementation of the finite element method which allows simulating partial differential equations in complex geometries.

Exploiting the radial symmetry of the problem, the simulation reduces to 2D by simulating on a plane through the pillar's center. The full nanopillar is simulated as a trapezoid to enable simulating angled wall profiles. The hollow nanopillar consists of the same trapezoid where the outer edges are thickened to a given value and the top edge is removed.

The weak form of Laplace's equation in vacuum with no source term is solved on the domain which consists of a square that is 10 times the height of the nanopillar in every dimension in order to minimize numerical edge effects. The boundary conditions are 0 Volt on the box edge, except for the bottom of the nanopillar. Every edge of the nanopillar is set to 1 Volt.

The electric field is computed by taking the gradient of the resulting voltage field in the x and y directions. The magnitude of the electric field is obtained by summing the square of the x and y components of the electric field. By interpolating the magnitude of the field spatially, we can compare the relative electric field magnitudes between the full and hollow nanopillars at the same locations (Supplementary Fig. 9).

Analysis of iAP data. All data analysis was automated and free of manual intervention. From a raw iAP trace recorded by either NEA or patch electrode, its corresponding standard deviation trace is calculated using a 1-ms sliding window. A peak finding algorithm subsequently identifies the peaks from the standard deviation trace, which correspond to the sharpest-rising points of individual iAPs. Then, the software examines the raw data trace to the left of each rising point to identify the starting point of each iAP, and to the right of each rising point to identify the maximum point of each iAP. The amplitude is calculated from the starting point to the maximum point. APD90 and APD50 are calculated as the width of the iAPs at 90 and 50 percent of repolarization. T_{rise} is the time that it takes from the 20 percent to the 80 percent of depolarization.

For scaling Patch and NEA recorded iAPs, the two recording traces are first time-aligned to the electroporation time and resampled to the same frequency of 2 kHz. Then, each trace is separately processed to identify the rising points of all iAPs. The software then automatically calculates a scaling factor for each pair of iAPs to account for their differences in amplitudes. This is done using the mean square error algorithm by first setting the mean of iAPs to 0 and normalizing the amplitude of the patch iAP to 1. Then, the scaling factor for the NEA iAP is calculated as $\text{sum}(iAP2 \cdot iAP1) / \text{sum}(AP2^2)$. After scaling, the deviation of the two iAP waveforms is calculated as the mean absolute deviation.

Pharmacology experiments. All pharmacology experiments were conducted using the following procedure. First, 4–6 cells were electroporated and iAP signals were obtained and recorded until a stable baseline was reached for all signals. In order to

obtain consistent recording files for all pharmacology experiments (such as the one shown in Fig. 6A), after the stable iAP baseline was reached, a new recording file was then started and continuously recorded for 30 min. At 20 s, DMSO was added as a control, followed by a sequential addition of increasing doses of the selected drug at 80 s, 280 s, 460 s and 640 s (as shown in Fig. 6A).

Data analysis for pharmacology experiments. Individual peaks were detected at and around time 75 s for the control data, and at 260 s, 440 s, 625 s, and 815 s for the four drug doses. The three action potentials closest to these timepoints were used for analysis. Differences in APD values between these three action potentials were usually under 1%. If AP signals at a low drug dose started to exhibit extracellular signatures, the data was not analyzed for higher drug doses. To overlay the iAPs at different drug doses, we time-aligned the traces to their sharp rising point with normalized amplitudes.

Reporting summary. Further information on research design is available in the Nature Research Reporting Summary linked to this article.

Data availability

The raw data that support the findings of this study have been deposited in the following google drive link: <https://drive.google.com/drive/folders/1VNJkzDY0OjxNbCOzYozcPISjT2LbWo1?usp=sharing>.

Code availability

The code to generate the voltage and electric field distributions based on the FEniCS Python package is available at https://github.com/bcuilab/Electric_Field_Lines. The Matlab code used for automated data analysis is available upon request.

Received: 15 October 2021; Accepted: 22 March 2022;

Published online: 26 April 2022

References

- Hondeghem, L. M. & Hoffmann, P. Blinded test in isolated female rabbit heart reliably identifies action potential duration prolongation and proarrhythmic drugs: importance of triangulation, reverse use dependence, and instability. *J. Cardiovasc. Pharmacol.* **41**, 14–24 (2003).
- Colatsky, T. et al. The comprehensive in vitro proarrhythmia assay (CiPA) initiative—update on progress. *J. Pharmacol. Toxicol. Methods* **81**, 15–20 (2016).
- Gibson, J. K., Yue, Y., Bronson, J., Palmer, C. & Numann, R. Human stem cell-derived cardiomyocytes detect drug-mediated changes in action potentials and ion currents. *J. Pharmacol. Toxicol. Methods* **70**, 255–267 (2014).
- Liang, P. et al. Drug screening using a library of human induced pluripotent stem cell-derived cardiomyocytes reveals disease-specific patterns of cardiotoxicity. *Circulation* **127**, 1677–1691 (2013).
- Crumb, W. J. Jr, Vicente, J., Johannesen, L. & Strauss, D. G. An evaluation of 30 clinical drugs against the comprehensive in vitro proarrhythmia assay (CiPA) proposed ion channel panel. *J. Pharmacol. Toxicol. Methods* **81**, 251–262 (2016).
- Hyun, S.-W., Kim, B.-R., Hyun, S.-A. & Seo, J.-W. The assessment of electrophysiological activity in human-induced pluripotent stem cell-derived cardiomyocytes exposed to dimethyl sulfoxide and ethanol by manual patch clamp and multi-electrode array system. *J. Pharmacol. Toxicol. Methods* **87**, 93–98 (2017).
- Scheel, O. et al. Action potential characterization of human induced pluripotent stem cell-derived cardiomyocytes using automated Patch-Clamp Technology. *Assay Drug Dev. Technol.* **12**, 457–469 (2014).
- Kramer, J. et al. Publisher Correction: Cross-site and cross-platform variability of automated patch clamp assessments of drug effects on human cardiac currents in recombinant cells. *Sci. Rep.* **10**, 11884 (2020).
- Dunlop, J., Bowlby, M., Peri, R., Vasilyev, D. & Arias, R. High-throughput electrophysiology: an emerging paradigm for ion-channel screening and physiology. *Nat. Rev. Drug Discov.* **7**, 358–368 (2008).
- Li, W. et al. Establishment of an automated patch-clamp platform for electrophysiological and pharmacological evaluation of hiPSC-CMs. *Stem Cell Res.* **41**, 101662 (2019).
- Stoelzle, S. et al. Automated patch clamp on mESC-derived cardiomyocytes for cardiotoxicity prediction. *J. Biomol. Screen.* **16**, 910–916 (2011).
- Hayes, H. B. et al. Novel method for action potential measurements from intact cardiac monolayers with multiwell microelectrode array technology. *Sci. Rep.* **9**, 11893 (2019).
- Lopez, C. M. et al. A multimodal CMOS MEA for high-throughput intracellular action potential measurements and impedance Spectroscopy in drug-screening applications. *IEEE J. Solid-State Circuits* **53**, 3076–3086 (2018).

14. Edwards, S. L. et al. A multiwell cardiac μ GMEA platform for action potential recordings from human iPSC-derived cardiomyocyte constructs. *Stem Cell Rep.* **11**, 522–536 (2018).
15. Abbott, J., Ye, T., Ham, D. & Park, H. Optimizing nanoelectrode arrays for scalable intracellular electrophysiology. *Acc. Chem. Res.* **51**, 600–608 (2018).
16. McGuire, A. F., Santoro, F. & Cui, B. Interfacing cells with vertical nanoscale devices: applications and characterization. *Annu. Rev. Anal. Chem.* **11**, 101–126 (2018).
17. Robinson, J. T. et al. Vertical nanowire electrode arrays as a scalable platform for intracellular interfacing to neuronal circuits. *Nat. Nanotechnol.* **7**, 180–184 (2012).
18. Xie, C., Lin, Z., Hanson, L., Cui, Y. & Cui, B. Intracellular recording of action potentials by nanopillar electroporation. *Nat. Nanotechnol.* **7**, 185–190 (2012).
19. Duan, X. et al. Intracellular recordings of action potentials by an extracellular nanoscale field-effect transistor. *Nat. Nanotechnol.* **7**, 174–179 (2011).
20. Hai, A., Shappir, J. & Spira, M. E. In-cell recordings by extracellular microelectrodes. *Nat. Methods* **7**, 200–202 (2010).
21. Angle, M. R., Cui, B. & Melosh, N. A. Nanotechnology and neurophysiology. *Curr. Opin. Neurobiol.* **32**, 132–140 (2015).
22. Spira, M. E. & Hai, A. Multi-electrode array technologies for neuroscience and cardiology. *Nat. Nanotechnol.* **8**, 83–94 (2013).
23. Desbiolles, B. X. E., de Coulon, E., Bertsch, A., Rohr, S. & Renaud, P. Intracellular recording of cardiomyocyte action potentials with nanopatterned volcano-shaped microelectrode arrays. *Nano Lett.* **19**, 6173–6181 (2019).
24. Desbiolles, B. X. E. et al. Nanovolcano microelectrode arrays: toward long-term on-demand registration of transmembrane action potentials by controlled electroporation. *Microsyst. Nanoeng.* **6**, 67 (2020).
25. Abbott, J. et al. A nanoelectrode array for obtaining intracellular recordings from thousands of connected neurons. *Nat. Biomed. Eng.* **4**, 232–241 (2020).
26. Abbott, J. et al. CMOS nanoelectrode array for all-electrical intracellular electrophysiological imaging. *Nat. Nanotechnol.* **12**, 460–466 (2017).
27. Liu, R. et al. High density individually addressable nanowire arrays record intracellular activity from primary rodent and human stem cell derived neurons. *Nano Lett.* **17**, 2757–2764 (2017).
28. Liu, R. et al. Ultra-sharp nanowire arrays natively permeate, record, and stimulate intracellular activity in neuronal and cardiac networks. *Adv. Funct. Materials* <https://doi.org/10.1002/adfm.202108378> (2021)
29. Lin, Z. C., Xie, C., Osakada, Y., Cui, Y. & Cui, B. Iridium oxide nanotube electrodes for sensitive and prolonged intracellular measurement of action potentials. *Nature Commun.* **5**, 5:3206 (2014).
30. Lin, Z. C. et al. Accurate nanoelectrode recording of human pluripotent stem cell-derived cardiomyocytes for assaying drugs and modeling disease. *Microsyst. Nanoeng.* **3**, 16080 (2017).
31. Dipalo, M. et al. Author Correction: Plasmonic meta-electrodes allow intracellular recordings at network level on high-density CMOS-multi-electrode arrays. *Nat. Nanotechnol.* **13**, 972 (2018).
32. Dipalo, M. et al. Intracellular action potential recordings from cardiomyocytes by ultrafast pulsed laser irradiation of fuzzy graphene microelectrodes. *Sci Adv* **7**, eabd5175 (2021).
33. Dipalo, M. et al. Intracellular and extracellular recording of spontaneous action potentials in mammalian neurons and cardiac cells with 3D plasmonic nanoelectrodes. *Nano Lett.* **17**, 3932–3939 (2017).
34. Broyles, C., Robinson, P. & Daniels, M. Fluorescent, bioluminescent, and optogenetic approaches to study excitable physiology in the single cardiomyocyte. *Cells* **7**, 51 (2018).
35. Dana, H. et al. High-performance calcium sensors for imaging activity in neuronal populations and microcompartments. *Nat. Methods* **16**, 649–657 (2019).
36. Shroff, S. N. et al. Voltage imaging of cardiac cells and tissue using the genetically encoded voltage sensor Archon1. *iScience* **23**, 100974 (2020).
37. Lou, H.-Y. et al. Membrane curvature underlies actin reorganization in response to nanoscale surface topography. *Proc. Natl Acad. Sci. USA* **116**, 23143–23151 (2019).
38. Zhao, W. et al. Nanoscale manipulation of membrane curvature for probing endocytosis in live cells. *Nat. Nanotechnol.* **12**, 750–756 (2017).
39. Burrige, P. W. et al. Chemically defined generation of human cardiomyocytes. *Nat. Methods* **11**, 855–860 (2014).
40. Ye, S. et al. Generation and expansion of human cardiomyocytes from patient peripheral blood mononuclear cells. *J. Vis. Exp.* <https://doi.org/10.3791/62206> (2021).
41. Zhu, R., Millrod, M. A., Zambidis, E. T. & Tung, L. Variability of action potentials within and among cardiac cell clusters derived from human embryonic stem cells. *Sci. Rep.* **6**, 18544 (2016).
42. Du, D. T. M., Hellen, N., Kane, C. & Terracciano, C. M. N. Action potential morphology of human induced pluripotent stem cell-derived cardiomyocytes does not predict cardiac chamber specificity and is dependent on cell density. *Biophys. J.* **108**, 1–4 (2015).
43. Strauss, D. G. et al. Comprehensive in vitro proarrhythmia assay (CiPA) update for a cardiac safety research consortium/Health and Environmental Sciences Institute/FDA Meeting. *Therapeutic Innov. Regulatory Sci.* **53**, 519–525 (2019).
44. Marschang, H., Beyer, T., Karolyi, L., Kübler, W. & Brachmann, J. Differential rate and potassium-dependent effects of the class III agents d-sotalol and dofetilide on guinea pig papillary muscle. *Cardiovasc. Drugs Ther.* **12**, 573–583 (1998).
45. Bayer, R., Rodenkirchen, R., Kaufmann, R., Lee, J. H. & Hennekes, R. The effects of nifedipine on contraction and monophasic action potential of isolated cat myocardium. *Naunyn. Schmiedeberg's Arch. Pharm.* **301**, 29–37 (1977).
46. Kimura, S., Bassett, A. L., Xi, H. & Myerburg, R. J. Verapamil diminishes action potential changes during metabolic inhibition by blocking ATP-regulated potassium currents. *Circ. Res.* **71**, 87–95 (1992).
47. Kohlhardt, M. & Haap, K. The response of Ca-mediated action potentials and contractile activity in mammalian ventricular myocardium towards alkalosis. *Experientia* **32**, 150–152 (1976).
48. Cedrini, L. & Alloati, G. Effect of temperature on the electrical and mechanical activity of lizard ventricular myocardium. *Boll. Soc. Ital. Biol. Sper.* **55**, 1362–1368 (1979).
49. Wu, H. et al. Modelling diastolic dysfunction in induced pluripotent stem cell-derived cardiomyocytes from hypertrophic cardiomyopathy patients. *Eur. Heart J.* **40**, 3685–3695 (2019).
50. Zhao, M.-T. et al. Molecular and functional resemblance of differentiated cells derived from isogenic human iPSCs and SCNT-derived ESCs. *Proc. Natl Acad. Sci. USA* **114**, E11111–E11120 (2017).

Acknowledgements

This work is supported by National Institutes of Health (1R35GM141598 (B.C.), 1R01NS121934 (B.C.), R01GM125737 (B.C.), R01HL155282 (M.T.Z.), R01HL145676 (J.C.W.), R01HL150693 (J.C.W.), and UH3TR002588 (J.C.W.)), American Heart Association (AHA) Career Development Award 18CDA34110293 (M.T.Z.), and Google LLC award (Z.J. and B.C.).

Author contributions

Z.J., Y.Y., C.T.T., and B.C. designed and conducted the experiments, analyzed data, and drafted the manuscript. E.P.F. and A.L. analyzed and interpreted the data and contributed to manuscript writing. A.F.M., C.F., H.Y., Z.Y., Z.J., M.T., W.Z., X.L., and T.L. assisted in experimental design and/or computational modeling and contributed to the methods section of the manuscript. A.P., J.C.W., and B.C. provided study oversight, J.C.W. and B.C. provided funding. All authors contributed to manuscript editing for the final version of the manuscript.

Competing interests

The authors declare no competing interests.

Additional information

Supplementary information The online version contains supplementary material available at <https://doi.org/10.1038/s41467-022-29726-2>.

Correspondence and requests for materials should be addressed to Bianxiao Cui.

Peer review information *Nature Communications* thanks Benoit Desbiolles for their contribution to the peer review of this work.

Reprints and permission information is available at <http://www.nature.com/reprints>

Publisher's note Springer Nature remains neutral with regard to jurisdictional claims in published maps and institutional affiliations.



Open Access This article is licensed under a Creative Commons Attribution 4.0 International License, which permits use, sharing, adaptation, distribution and reproduction in any medium or format, as long as you give appropriate credit to the original author(s) and the source, provide a link to the Creative Commons license, and indicate if changes were made. The images or other third party material in this article are included in the article's Creative Commons license, unless indicated otherwise in a credit line to the material. If material is not included in the article's Creative Commons license and your intended use is not permitted by statutory regulation or exceeds the permitted use, you will need to obtain permission directly from the copyright holder. To view a copy of this license, visit <http://creativecommons.org/licenses/by/4.0/>.

© The Author(s) 2022